

Comparison of novel regularization techniques in seismic tomography

I. Loris¹, H. Douma², G. Nolet³, I. Daubechies⁴, C. Regone⁵

¹Mathematics Department, Vrije Universiteit Brussel, E-mail: igloris@vub.ac.be

²Department of Geosciences, Princeton University

³Geosciences Azur, Université de Nice-Sophia Antipolis,
CNRS/IRD/Université Pierre et Marie Curie

⁴Program in Applied and Computational Mathematics, Princeton University

⁵BP America Inc., 501 Westlake Park Blvd, Houston, TX 77079

October 29, 2018

Abstract

The performance of several recent and existing regularization techniques are compared in the framework of 3D seismic tomography. These include traditional ℓ_2 penalties, but also a sparsity promoting ℓ_1 penalty and a total variation penalty. Which of these algorithms is judged optimal depends on the specific requirements of the scientific experiment. If the correct reproduction of model amplitudes is important, classical damping towards a smooth model using an ℓ_2 norm works almost as well as minimizing the total variation but is much more efficient. If gradients (edges of anomalies) should be resolved with a minimum of distortion, we prefer ℓ_1 damping of Daubechies-4 wavelet coefficients. Simple ℓ_2 minimization (‘Tikhonov regularization’) should be avoided.

1 Introduction

Since geophysical inverse problems are almost always underdetermined, regularization techniques are essential to obtain a meaningful solution. Two major classes of techniques exist. The first one, named ‘mollifying’ in the mathematical literature, or ‘optimally localized averaging’ (OLA) in helioseismology, can be traced back to the groundbreaking work of Backus and Gilbert (Backus & Gilbert, 1967, 1970) in geophysics. In this approach one searches for the size of an averaging volume that can produce a local average of the model parameter with an acceptable variance. Since this method is computationally very expensive, it has found little application in large-scale geophysical inversions such as seismic tomography. To limit the computational effort, seismic tomographers instead search for a biased (‘damped’) solution. This has the disadvantage of introducing a systematic error – the bias – in lieu of the random error caused by the propagation of data errors. It can be turned into an advantage if the bias actually reflects a justified disposition of the scientist to prefer certain models over others, as long as the data are fit within their error bars.

Simple ℓ_2 -norm damping, which biases model perturbations towards zero in the absence of information based on the data, is generally a bad choice to regularize the inverse problem for seismic tomography as it tends to introduce structures reflecting ray coverage into the images. For that reason, most tomographers prefer to bias the model towards ‘smooth’

anomalies, in effect trying to forge a compromise between Backus-Gilbert theory and the efficiency of damped inversions. The smoothness of the images has the advantage that large structures become easily visible. Sharp discontinuities, however, are blurred, and smaller structures, even when resolved, may be diluted beyond recognition. Recently, Loris et al. (2007) — hereafter referred to as Paper I — introduced a third option for the bias: to minimize the ℓ_1 -norm of the wavelet decomposition. In a synthetic 2D experiment using surface wave data, we showed how structurally coherent features (in a geophysical sense), were more faithfully reproduced using this technique than with a simple ℓ_2 -norm damping. In this paper we extend this test to 3D inversions of body wave travel times, investigate the use of different families of wavelets, and include a comparison with smoothness damping, and with a fourth option named ‘total variation’ damping. The (salt dome) model is more realistic and includes a wide range of length scales.

The problem described in Paper I was of a limited size: there were about 10^4 degrees of freedom in the reconstructed models. In this paper we make 3D reconstructions, and increase the number of degrees of freedom by an order of magnitude to about $\sim 10^5$. The number of data also increases accordingly to 24000.

Our approach is complementary to that of Chevrot & Zhao (2007) who expand the Fréchet kernels into wavelets to obtain a significant reduction in the memory requirements to store the kernel.

One disadvantage of ℓ_1 -norm methods is that they lack the convenient linearity of the more conventional ℓ_2 -norm minimizations. In this paper we report on our investigations of different reconstruction algorithms and their performance.

2 Problem formulation

2.1 Forward problem

We test the regularization on a synthetic data set generated for a realistic salt dome model. Since the main goal of this paper is to test and compare a large number of algorithms, numerical efficiency is more important than the wish to have a tomographic problem at hand that is fully realistic. We have thus taken a few shortcuts to be able to run inversions quickly in Matlab on a single processor. However, we took pains to ensure that we would invert for a model that has a large range of length scales, and that the ray coverage would encompass both dense and sparse regions.

In dimensionless variables, the expression for a finite frequency sensitivity kernel corresponding to a constant background and a Gaussian power spectrum is given by the formula:

$$K(x, y, z) = \frac{e^{-u^2} H_5(u)}{24\lambda d_s d_r} \quad , \quad (1)$$

where $u = \pi(d_s + d_r - d_{sr})/\lambda$. Here d_{sr} is the distance between source and receiver, and d_s, d_r are the distances to source and to receiver, measured from the point (x, y, z) . λ is the dominant wavelength and $H_5(u) = 120u - 160u^3 + 32u^5$ denotes the Hermite polynomial of order 5. Equation (1) can easily be derived from the expressions for the Fréchet kernel in a homogeneous medium using an analytical expression for the spectral integration; see (Nolet, 2008, section 7.8) or (Dahlen, 2004, equations (5,6,7)).

For each source-receiver pair and each dominant wavelength, the travel time differential

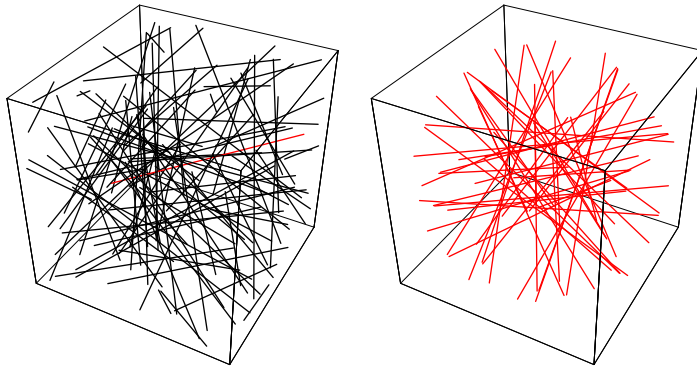


Figure 1: Left: The cube $[-1, 1]^3$ with the initial 100 source-receiver pairs, joined by a straight line. One ray is singled out in red. Right: 48 rays generated by the 48 symmetry transformations of the cube from the single red ray in the left pane. Plotting all 4800 rays obtained in this way would fill the whole cube.

and the model perturbation \mathbf{m} are connected by the linear integral relation

$$\delta T = \int_V K \mathbf{m} dV. \quad (2)$$

Given sufficiently many data, the aim of seismic tomography is to reconstruct the model \mathbf{m} from a noisy version of the data \mathbf{d} .

In section 3 we will perform a number of seismic reconstructions. The domain on which we will do this is the cube $[-1, 1]^3$. For discretization, this domain is subdivided in 64^3 voxels leading to 262144 degrees of freedom in our model. Voxels are a convenient choice for the digital reconstruction of a model \mathbf{m} . In order to be able to produce meaningful reconstructions, we expect to need about 10^4 data (about 1 datum for 10 degrees of freedom). Hence we will choose 4800 sources-receiver pairs and 5 different dominant wavelengths so as to come to 24000 data. This represents an overparametrization by a factor of more than 10. Thus regularization is an essential requirement for any data inversion.

We first choose 100 source-receiver pairs in random positions on the surface of the cube, while making sure source and receiver are never on the same face. From these starting 100 pairs, we construct the full set of 4800 pairs by using the 48 symmetry transformations of the cube. These 48 operations are constructed from the $3!$ permutations of the coordinates (x, y, z) , and by the 2^3 reflections $(\pm x, \pm y, \pm z)$. The initial 100 source receiver pairs and the 48 transformations of the cube are depicted in figure 1.

For each of the 4800 source-receiver pairs we will construct 5 finite frequency sensitivity kernels (1) corresponding to 5 different dominant wavelengths $\lambda = \{0.5, 0.2, 0.08, 0.04, 0.025\}$. Thus, in total there will be 24000 kernels at our disposal. Because of the symmetry transformations used and the random choice of the initial 100 source-receiver pairs, the coverage of the domain by these 24000 kernels is quite uniform (see figure 2).

In addition we construct a second operator containing only 20000 out of the 24000 kernels. We chose to remove the 4000 kernels for which the line connecting source and receiver comes closest to the point $(0.24, -0.7, -0.23)$. In this way, we end up with an operator that has a hole in its coverage of the cube (see figure 2, right), and we will be able to demonstrate the effect of non-uniform coverage.

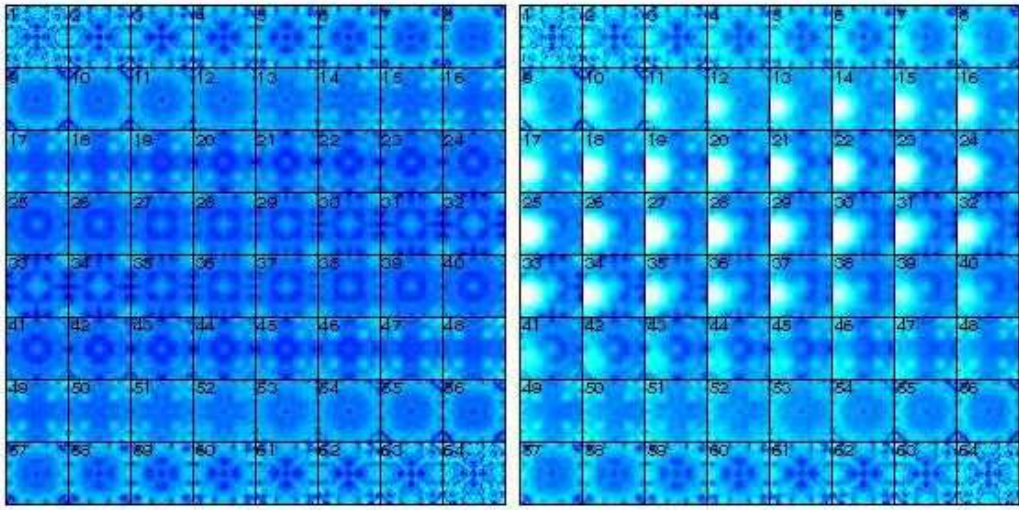


Figure 2: Left: Visualization of the coverage of the domain by 24000 sensitivity kernels (see text) in the operator \mathbf{A} , by means of a plot of $\sum_i |A_{ij}|$, the sum of the absolute values of the sensitivity kernels at location j . Right: Same plot for the operator built from 20000 sensitivity kernels (see text). The cube of 64^3 voxels is divided in 64 horizontal slices and these slices are displayed next to each other. Number 1 is the top slice, and number 64 is the bottom slice. The geometric pattern visible in both depictions is a remnant of the 48 symmetry transformations used to build the set of kernels. In both plots light blue regions correspond to smaller value of $\sum_i |\mathbf{A}_{ij}|$ than dark blue regions; white corresponds to zero. (Note: The arXiv version of this picture uses JPEG compression)

To minimize the error due to discretization of the model into voxels we calculate the integral of the sensitivity kernels over each voxel (using a Riemann sum with 4^3 terms/voxel) for each source-receiver pair and each of the five dominant wavelengths we consider. The resulting values make up the operator \mathbf{A} we want to invert: Because there are 24000 kernels and $64^3 = 262144$ voxels, the matrix \mathbf{A} will have 24000 rows (one row per kernel) and 262144 columns (one column per voxel in the model).

The use of the 48 symmetry transformations of the cube allows us to save a factor of 48 in memory requirements for our calculations. I.e. we need to compute and store only 500 kernels corresponding to the original 100 source-receiver pairs. The remaining ones are easily (and quickly) generated from these initial 500 kernels by the symmetry transformations of the cube. Though not realistic, this configuration of rays provides for an easy way to compare dense and partial data coverage of the model.

An additional saving in memory requirements is obtained by exploiting the fact that most kernels are well localized (i.e. they are thin), and thus that the A_{ij} are practically zero for many voxels. In other words, each row of the matrix \mathbf{A} is relatively sparse.

2.2 Reconstruction methods

Reconstructing the model \mathbf{m} from the data \mathbf{d} is done by solving the linear system $\mathbf{A}\mathbf{m} = \mathbf{d}$, where \mathbf{A} denotes, as before, the matrix containing the kernels discretized in the voxel basis. This system may contain incompatible equations (due to noise), and, at the same time, be underdetermined (not enough data to reconstruct all of \mathbf{m}). The problem of incompatible data can be solved by replacing problem $\mathbf{A}\mathbf{m} = \mathbf{d}$ with the minimization of a data fidelity term:

$$\bar{\mathbf{m}} = \arg \min_{\mathbf{m}} \|\mathbf{A}\mathbf{m} - \mathbf{d}\|^2. \quad (3)$$

Although a minimizer always exists (because of the quadratic nature of the functional), it may not always be unique. In other words, the problem is still underdetermined and an iterative numerical scheme for finding a minimizer of (3) may diverge.

We therefore augment the functional in (3) by a term that will penalize a whole category of models that is thought to be unphysical. The prime example of this kind of method is Tikhonov regularization (Tikhonov, 1963) whereby a penalty proportional to the ℓ_2 -norm of the model is imposed:

$$\bar{\mathbf{m}} = \arg \min_{\mathbf{m}} \|\mathbf{A}\mathbf{m} - \mathbf{d}\|^2 + \mu \|\mathbf{m}\|^2. \quad (4)$$

This will effectively prevent the model from growing unboundedly due to noise in \mathbf{d} and ill-conditioning of the matrix \mathbf{A} .

Another, closely related, possibility is to impose a penalty consisting of the ℓ_2 -norm of the (discrete) Laplacian $\Delta\mathbf{m}$ of \mathbf{m} :

$$\bar{m} = \arg \min_m \|\mathbf{A}\mathbf{m} - \mathbf{d}\|^2 + \mu \|\Delta\mathbf{m}\|^2. \quad (5)$$

As we will see in section 3, this will enforce a certain degree of smoothness on the reconstructed model. The Laplacian used here is defined as the difference of the model with the local average over the six nearest neighbors: $(\Delta\mathbf{m})_{ijk} = \mathbf{m}_{ijk} - (\mathbf{m}_{i-1jk} + \mathbf{m}_{i+1jk} + \dots + \mathbf{m}_{ijk+1})/6$.

The above two versions of the Tikhonov regularization method have the advantage of being solvable by linear equations. The variational equations that determine the minimizers of (4) and (5) are:

$$\mathbf{A}^T \mathbf{A} \mathbf{m} + \mu \mathbf{m} = \mathbf{A}^T \mathbf{d}, \quad (6)$$

and

$$\mathbf{A}^T \mathbf{A} \mathbf{m} + \mu \Delta^T \Delta \mathbf{m} = \mathbf{A}^T \mathbf{d}, \quad (7)$$

respectively (with suitable treatment of boundary voxels, $\Delta^T = \Delta$). For these linear equations, we can use the conjugate gradient algorithm. With $\mathbf{m}^{(0)}$ arbitrary and $\mathbf{r}^{(n)} = \mathbf{A}^T (\mathbf{d} - \mathbf{A} \mathbf{m}^{(n)}) - \lambda \mathbf{D}^T \mathbf{D} \mathbf{m}^{(n)}$, we set

$$\begin{aligned} \mathbf{v}^{(n)} &= \begin{cases} \mathbf{r}^{(n)} & n = 0 \\ \mathbf{r}^{(n)} + \frac{\|\mathbf{r}^{(n)}\|^2}{\|\mathbf{r}^{(n-1)}\|^2} \mathbf{v}^{(n-1)} & n > 0 \end{cases} \\ \mathbf{m}^{(n+1)} &= \mathbf{m}^{(n)} + \frac{\|\mathbf{v}^{(n)}\|^2}{\|\mathbf{A} \mathbf{v}^{(n)}\|^2 + \mu \|\mathbf{D} \mathbf{v}^{(n)}\|^2} \mathbf{v}^{(n)} \end{aligned} \quad (8)$$

where \mathbf{D} is either the unit matrix \mathbf{I} (in case we use functional (4)) or Δ (in case we use functional (5)). The model estimates $\mathbf{m}^{(n)}$ converge to the minimizer (4) or (5), respectively.

Another method of regularization consists of imposing an ℓ_1 -norm penalty (Daubechies et al., 2004). It can be shown that this leads to a sparse model, i.e. a model with few nonzero components (Donoho, 2006a,b). It would therefore not be a good idea to apply this technique on the model in the voxel basis (there is no reason to assume the model would be sparse in that basis); we would rather use this penalty on the coefficients of the model in a different basis in which we believe the model to be sparse.

Harmonic functions would allow us to select resolvable scales, but the complete lack of localisation of these functions makes them even worse candidates than voxels. 3D wavelets offer a compromise between the concentration of power in both scale and location, and are intuitively more suitable to build (geophysically) reasonable models. In fact, our earlier experience (Paper 1) showed the advantages of using a wavelet basis, and constructing the model using:

$$\bar{\mathbf{m}} = \mathbf{W}^{-1} \bar{\mathbf{w}} \quad \text{and} \quad \bar{\mathbf{w}} = \arg \min_{\mathbf{w}} \|\mathbf{A} \mathbf{W}^{-1} \mathbf{w} - \mathbf{d}\|^2 + 2\mu \|\mathbf{w}\|_1 \quad (9)$$

Here, \mathbf{w} denotes the (vector of) wavelet coefficients of the model, \mathbf{W} is the wavelet decomposition matrix and \mathbf{W}^{-1} the wavelet synthesis operator. This type of penalty leads to a model that has a sparse wavelet representation, i.e. a model with (very) few nonzero wavelet coefficients. The aim is thus to rely on the properties of the wavelet basis to be able to represent the desired solution with few nonzero components. In geophysics wavelets are a good choice for seismic reconstruction as they allow for sparse representations of overall smooth functions, while still capable of taking into account the possibility of isolated sharp features (Daubechies, 1992; Loris et al., 2007). In section 3, we shall consider a number of different choices of (orthonormal) wavelet bases. For each of these choices, we have $\mathbf{W}^{-1} = \mathbf{W}^T$, which we will implicitly assume hereafter.

In order to find the minimizer $\bar{\mathbf{w}}$ of the ℓ_1 penalized functional (9), one may use the iterative soft-thresholding algorithm (Daubechies et al., 2004):

$$\mathbf{w}^{(n+1)} = \mathcal{S}_{\alpha\mu} \left[\mathbf{w}^{(n)} + \alpha \mathbf{W} \mathbf{A}^T (\mathbf{d} - \mathbf{A} \mathbf{W}^T \mathbf{w}^{(n)}) \right], \quad (10)$$

$\mathbf{w}^{(0)}$ may be chosen arbitrarily. The soft-thresholding function operates component-wise and is defined by

$$\mathcal{S}_\tau(u) = \begin{cases} u - \tau & u \geq \tau \\ 0 & |u| \leq \tau \\ u + \tau & u \leq -\tau \end{cases} . \quad (11)$$

The constant α should be chosen such that $\alpha\|\mathbf{A}^T\mathbf{A}\|$ is smaller than or 1 (Daubechies et al., 2004) ($\|\mathbf{A}^T\mathbf{A}\|$ is defined as the largest eigenvalue of $\mathbf{A}^T\mathbf{A}$). The wavelet transform \mathbf{W} and its inverse \mathbf{W}^T are fast transforms. This means that they cost only a fraction of the computer time needed to perform one application of \mathbf{A} or \mathbf{A}^T . In other words, working in a wavelet basis does not significantly change the computational complexity of the reconstruction algorithm. This technique has already been used in 2D seismic tomography in Paper I.

A final penalty term we will consider is the so-called ‘total variation’ (TV) penalty:

$$\bar{\mathbf{m}} = \arg \min_{\mathbf{m}} \|\mathbf{A}\mathbf{m} - \mathbf{d}\|^2 + 2\mu \sum_{ijk} \sqrt{(\Delta_x\mathbf{m})^2 + (\Delta_y\mathbf{m})^2 + (\Delta_z\mathbf{m})^2} \quad (12)$$

with $\Delta_x\mathbf{m} = \mathbf{m}_{ijk} - \mathbf{m}_{i-1jk}$ and similarly for Δ_y and Δ_z . This penalization will favor piecewise constant models (in the voxel basis). Unfortunately, the equations that determine the minimizer (12) are nonlinear.

In this work, we use a reweighed conjugate gradient method (Bioucas-Dias et al., 2006) to determine the minimum of the TV functional (12). More specifically, defining the weights $\mathbf{u}^{(n)} = (\Delta_x\mathbf{m}^{(n)} + \Delta_y\mathbf{m}^{(n)} + \Delta_z\mathbf{m}^{(n)})^{-1/2}$, we shall use algorithm (8) where we choose $\mathbf{D}^T\mathbf{D} = \Delta_x^T\mathbf{u}^{(n)}\Delta_x + \Delta_y^T\mathbf{u}^{(n)}\Delta_y + \Delta_z^T\mathbf{u}^{(n)}\Delta_z$ (which depends on the iteration n) and use that $\|\mathbf{D}\mathbf{v}^{(n)}\| = \langle \mathbf{D}^T\mathbf{D}\mathbf{v}^{(n)}, \mathbf{v}^{(n)} \rangle$. Because of the non-quadratic nature of functional (12), the conjugate gradient algorithm no longer preserves conjugacy between successive search directions $\mathbf{v}^{(n)}$ as n grows. For this reason, the iteration is also reset every so often (in accordance with (Bioucas-Dias et al., 2006)).

As such, the minimizers defined by (4), (5) and (9) still depend on the penalty parameter μ . In the reconstructions below, we fix this parameter by requiring that the reconstructed solution $\bar{\mathbf{m}}$ fits the data \mathbf{d} as well as possible, but not any better than the noise level:

$$\|\mathbf{A}\bar{\mathbf{m}} - \mathbf{d}\| \approx \|\mathbf{n}\|, \quad (13)$$

with \mathbf{n} representing the noise vector. In other words, the discrepancy principle tells us to choose the penalty parameter μ such that

$$\|\mathbf{A}\bar{\mathbf{m}} - \mathbf{d}\|^2/\sigma^2 \approx \text{number of data} \quad (14)$$

where σ is the noise variance (if different data have different variance, it is simplest to divide from the outset each row as well as the right hand side by the standard deviation of its datum, and set $\sigma = 1$ in (14)). In practice, this means that we will have to perform the minimization several times, until a suitable value of μ is determined.

The above three numerical algorithms —conjugate gradient, iterative soft-thresholding and reweighed conjugate gradient— all need one application of \mathbf{A} and one application of \mathbf{A}^T per iteration step. Hence, it is sufficient to compare the number of iterations when we evaluate the efficiency of different reconstructions in the next section.

3 Reconstructions

In this section we present some sample reconstructions using the algorithms mentioned in section 2.2, applied to the finite frequency tomography problem described in section 2.1. We will consider a simple checkerboard input model that we will try to reconstruct from

incomplete and noisy data. We will also look at a more complicated salt dome model which we obtained from BP America, Inc.

In each case, our procedure will be the following. We start from a known input model $\mathbf{m}^{\text{input}}$ from which we construct synthetic noisy data \mathbf{d} :

$$\mathbf{d} = \mathbf{A}\mathbf{m}^{\text{input}} + \mathbf{n} \quad (15)$$

The noise n is taken from a Gaussian distribution, with zero mean and variance σ chosen in such a way that $\|\mathbf{n}\|/\|\mathbf{A}\mathbf{m}^{\text{input}}\| = 0.1$; in other words, we add 10% noise to the noiseless data. The goal is then to try to reconstruct $\mathbf{m}^{\text{input}}$ as well as possible from \mathbf{d} and \mathbf{A} . For this we will use methods (4), (5), (9) and (12), and compare their performance. Since we know the noise variance σ , we can use the criterion (14) to choose the penalty parameter μ

For the wavelet based method (9), we also need to choose a wavelet family. There are many wavelet bases, with various degrees of smoothness and approximation properties (Daubechies, 1992). Because we use wavelets together with an ℓ_1 penalty to render the model sparse, we will adapt our choice of basis to the input model. In particular, for the checkerboard reconstruction we will use Haar wavelets. For the salt dome input model, we will compare the effect of different choices of wavelets bases on the reconstruction. Our choice will include Haar wavelets, D4 wavelets and also directional dual tree wavelets.

In all cases, we start the iterative reconstruction algorithms from $\mathbf{w}^{(0)} = 0$ or $\mathbf{m}^{(0)} = 0$.

3.1 Checkerboard

The first example consists of a checkerboard pattern; in other words the input model $\mathbf{m}^{\text{input}}$ is piecewise constant (± 1) on small cubes of 8 by 8 by 8 voxels. It mainly serves as a proof of principle for the ℓ_1 wavelet method (9) because we know that this input model is sparse in the Haar wavelet basis (Haar, 1910). In fact, it only has 99 nonzero coefficients in that basis. Hence, we may expect that the ℓ_1 method will work very well in this basis.

The input model and four reconstructions are shown in figure 3 (with the same way of representing the 3D information as in figure 2). All reconstructions use all 24000 kernels and thus have near uniform coverage (see figure 2). The ℓ_1 reconstruction with Haar wavelets is visually, by far, the most faithful to the original. The ℓ_2 -reconstructions and the TV reconstruction display smooth transitions between +1 and -1. The reconstruction result of the simple ℓ_2 method (4) is the most noisy of all.

The number of iterations and corresponding relative reconstruction errors $\|\mathbf{m} - \mathbf{m}^{\text{input}}\|/\|\mathbf{m}^{\text{input}}\|$ are also listed in figure 3. They show that the ℓ_1 method does extraordinarily well in this case. The total variation minimization and the Laplacian penalization perform better than the simple ℓ_2 method.

The smoothing effect of the reconstructions can quantitatively be seen from the histogram of the reconstructed model amplitudes (see figure 4). The ℓ_2 reconstruction takes on mostly values around zero, whereas the input model only has amplitudes +1 and -1 (vertical blue lines). In this case, the ℓ_1 -Haar reconstruction does a very good job at recovering the ± 1 amplitude distribution, as it is naturally well suited for the particular checkerboard model used.

3.2 A 3D salt dome model

In this section we try to reconstruct a complex 3D model of a realistic salt body in the subsurface. The complex salt-dome model was obtained from a prestack depth-migration

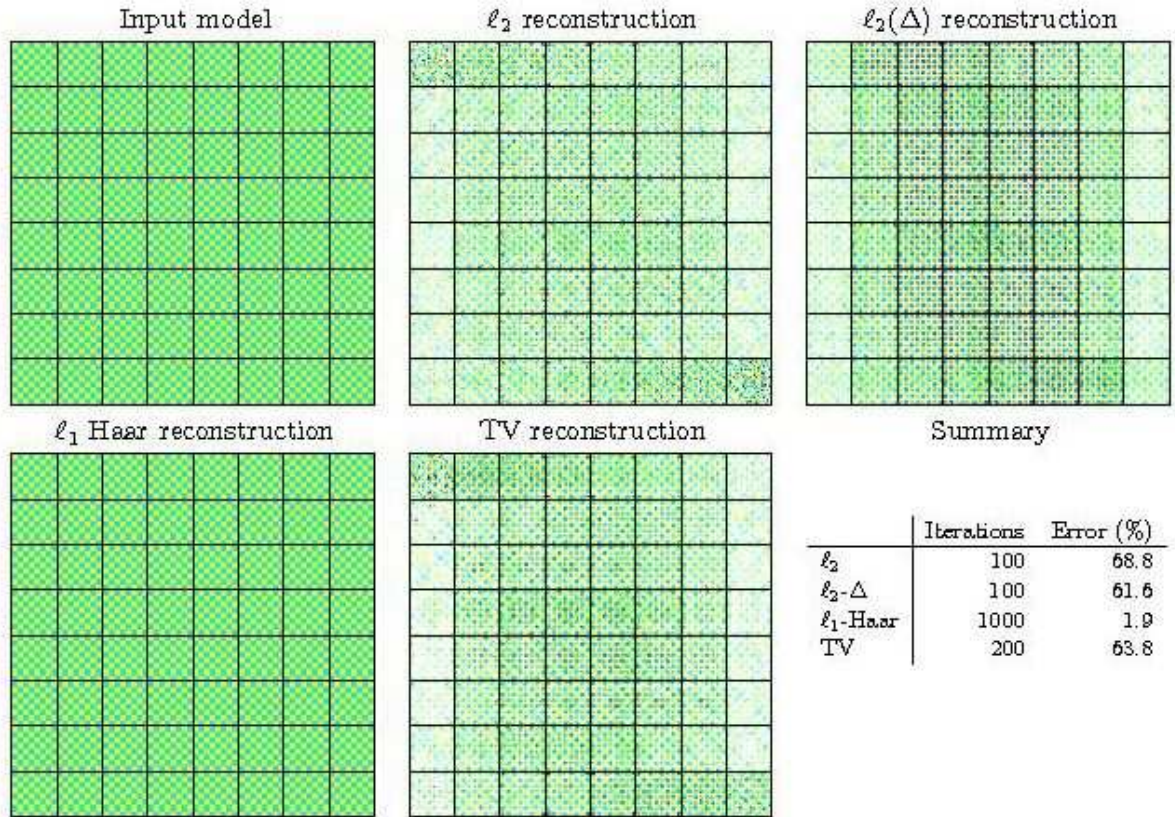


Figure 3: The checkerboard model and its reconstructions using all 24000 data. The models are represented in the same way as in figure 2, except that the numbering of the slices is omitted here. The whitish transitions in several of the reconstructions are the result of smoothing between $+1$ and -1 of the input model. As the input checkerboard has fields of size $8 \times 8 \times 8$ with constant model value ± 1 , the smoothing also occurs with period 8 in all three directions. In particular, slices 8-9, 16-17, ... are mostly white in the ℓ_2 and TV reconstructions. (Note: The arXiv version of this picture uses JPEG compression)

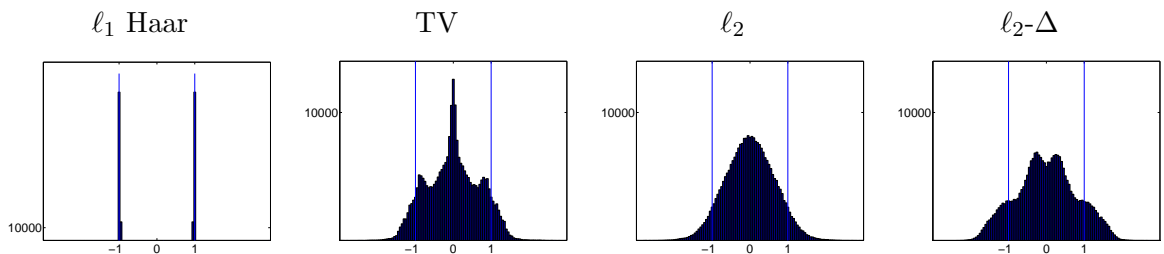


Figure 4: Histograms of the amplitude distribution of the four checkerboard reconstructions. The input model takes on values $+1$ and -1 only (thin blue lines in the four figures). The ℓ_1 reconstruction in the Haar basis results in almost perfect reconstruction of the amplitude distribution whereas for the other reconstruction methods the amplitudes are shifted towards zero.

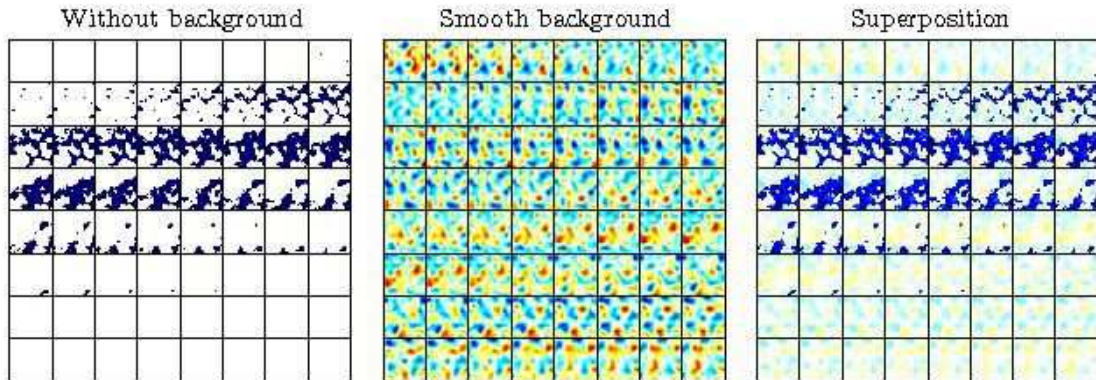


Figure 5: The model is constructed by adding both a salt dome model (left), and a long wavelength perturbation (center) to the homogeneous background model. The long wavelength perturbation was generated by smoothing a random field of Gaussian velocity perturbations. The amplitude of the Gaussian background is $1/3$ of the amplitude of the model on the left. (Note: The arXiv version of this picture uses JPEG compression)

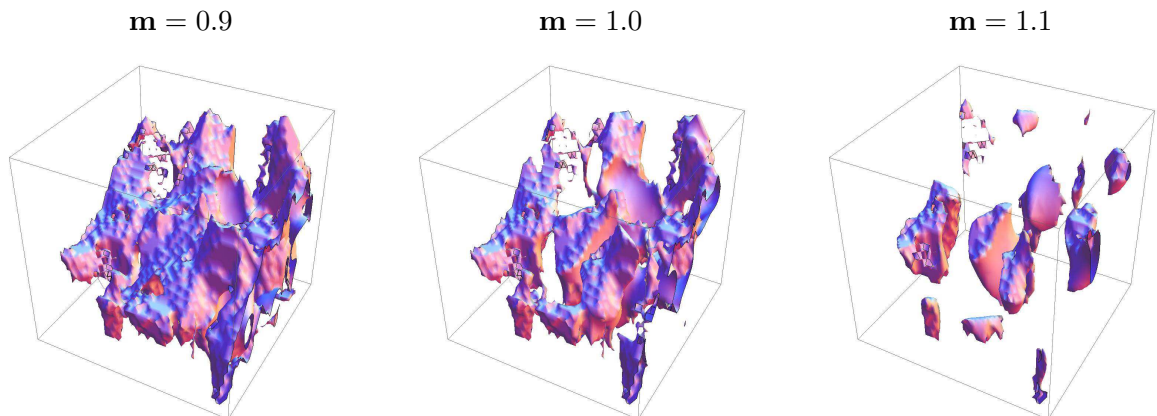


Figure 6: A depiction of three level sets of the salt dome model ($m = 0.9, 1.0, 1.1$).

of field seismic data in the deep-water part of the Gulf of Mexico. This model was kindly provided to us by BP America, Inc. To better accommodate the straight-ray tomography used in this paper, the sediment velocities surrounding the salt-dome model that were present in the original model provided to us, were replaced with a constant velocity. The resulting model is shown in Figure 5 (left) and we refer to this model as the noise-free model. This model was superimposed on a background model with long-wavelength variations (smoothed Gaussian). The noise-free model (with values 0, 1), the background and their superposition are shown in figure 5. The model has a rather sharp contrast between the velocity in the salt and in the surrounding background model, providing for sharp edges. Three level-set pictures of this model are shown in figure 6, corresponding to the levels $m = 0.9$, $m = 1$ and $m = 1.1$. The model contains $64 \times 64 \times 64 = 262144$ voxels as in the checkerboard examples. This sampling was achieved by a simple subsampling of the original model that had $1605 \times 1416 \times 513 \approx 10^9$ voxels, i.e., model parameters.

We perform the same type of experiment as before: we construct synthetic data and add 10% Gaussian noise to it. From this noisy data, we try to reconstruct the input model.

There are two differences with the checkerboard reconstructions. Firstly, we will compare several different wavelet families for the ℓ_1 reconstruction (in this case, there is no obvious reason to prefer Haar wavelets over other wavelet bases). Secondly, we will repeat the reconstruction experiment for an operator that has only 20000 kernels instead of 24000, to simulate imperfect coverage of the model by the kernels (a region of the model is ill resolved).

The wavelet families used are, in order of increasing smoothness: Haar (Haar, 1910), D4 on the interval (Cohen et al., 1992, 1993) and so-called directional dual tree (DT) wavelets (Kingsbury, 1999, 2002). The Haar and D4 wavelet transform on the cube are direct products of the corresponding wavelet transforms in 1D. The DT wavelet transform is not and it has, by construction, better directional sensitivity.

Judging the success of an algorithm to reconstitute the input model invariably involves a degree of subjectiveness, even if one designs a numerical measure for goodness of model fit. Such measure might also depend on the goal of the scientific experiment conducted. For example, if one deducts temperatures from velocity variations, it is more important that the amplitudes are correct and less important that sharp edges of an anomaly are preserved, but a structural geologist may be more interested in the edges and wish to involve the misfit of the gradient, for example. In the figures, we list the amplitude misfit ($\|\mathbf{m} - \mathbf{m}^{\text{input}}\|/\|\mathbf{m}^{\text{input}}\|$) and judge the fit to other features visually.

For the reconstruction using all 24000 kernels, the TV method works best based on the final resulting error, as well as visual inspection (see figure 7). It is closely followed by the ℓ_1 method using dual tree wavelets (ℓ_1 -DT) and by the ℓ_2 method with Laplacian smoothing (ℓ_2 - Δ). The ℓ_1 method with D4 wavelets does better than with Haar wavelets, and the worst result is obtained using the simple ℓ_2 penalized method. However, the ‘‘top three’’ methods (TV, ℓ_1 -DT, ℓ_2 - Δ) produce much smoother models than the input model. In case the correct sharpness of features is a desirable characteristic of the solution, the ℓ_1 reconstructions with Haar or D4 wavelets are more faithful to the input data. In this case one may well prefer D4 over Haar to avoid the rather blocky nature of the shapes. A blow-up of a single horizontal slice (number 25) of the different reconstructions is pictured in figure 8.

In case of the reconstructions with only 20000 kernels (figure 9), we see that simple ℓ_2 penalty again performs the worst, closely followed by the ℓ_1 -Haar method, just like in the case of uniform coverage using all 24000 kernels. The best result is for the ℓ_2 - Δ method, with the ℓ_1 -DT method in close second place. The TV and ℓ_1 -D4 methods are in between.

But the most interesting comparisons are again done visually. The lack of data coverage affects most strongly the lower left corner of levels 13–44 (third and fourth row in Fig. 9 especially). Not surprisingly, none of the algorithms is able to ‘recreate’ the model where there are no data at all. But close inspection of the model near the edge of the region affected by the data gap shows that the Haar and D4 wavelets produce the model that is least contaminated by smoothing effects beyond the gap, with D4 occasionally trying to correctly ‘fill in’.

4 Conclusions

In Paper 1 we showed how a large scale anomaly could be reconstituted even where it was ill resolved because of the selective nature of the wavelet coefficients and the ℓ_1 criterion: one wavelet coefficient reconstituting a large, circular, anomaly gave a better optimization than a couple of coefficients reconstituting only the resolved part. With the results of the

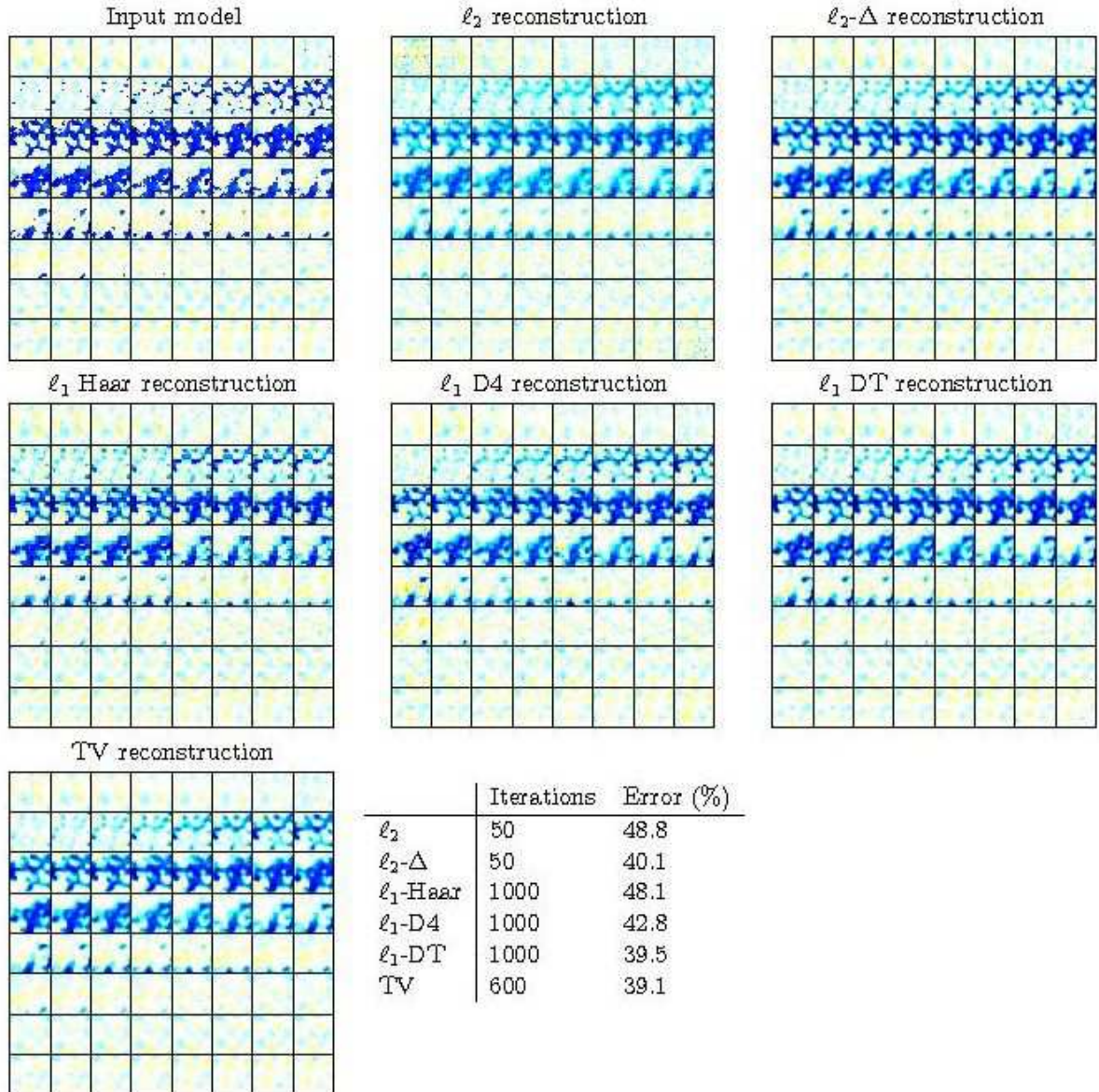


Figure 7: The salt dome model and its reconstructions using all 24000 kernels and thus near-uniform coverage. The TV method performs best, closely followed by the ℓ_1 -DT and ℓ_2 - Δ methods. (Note: The arXiv version of this picture uses JPEG compression)

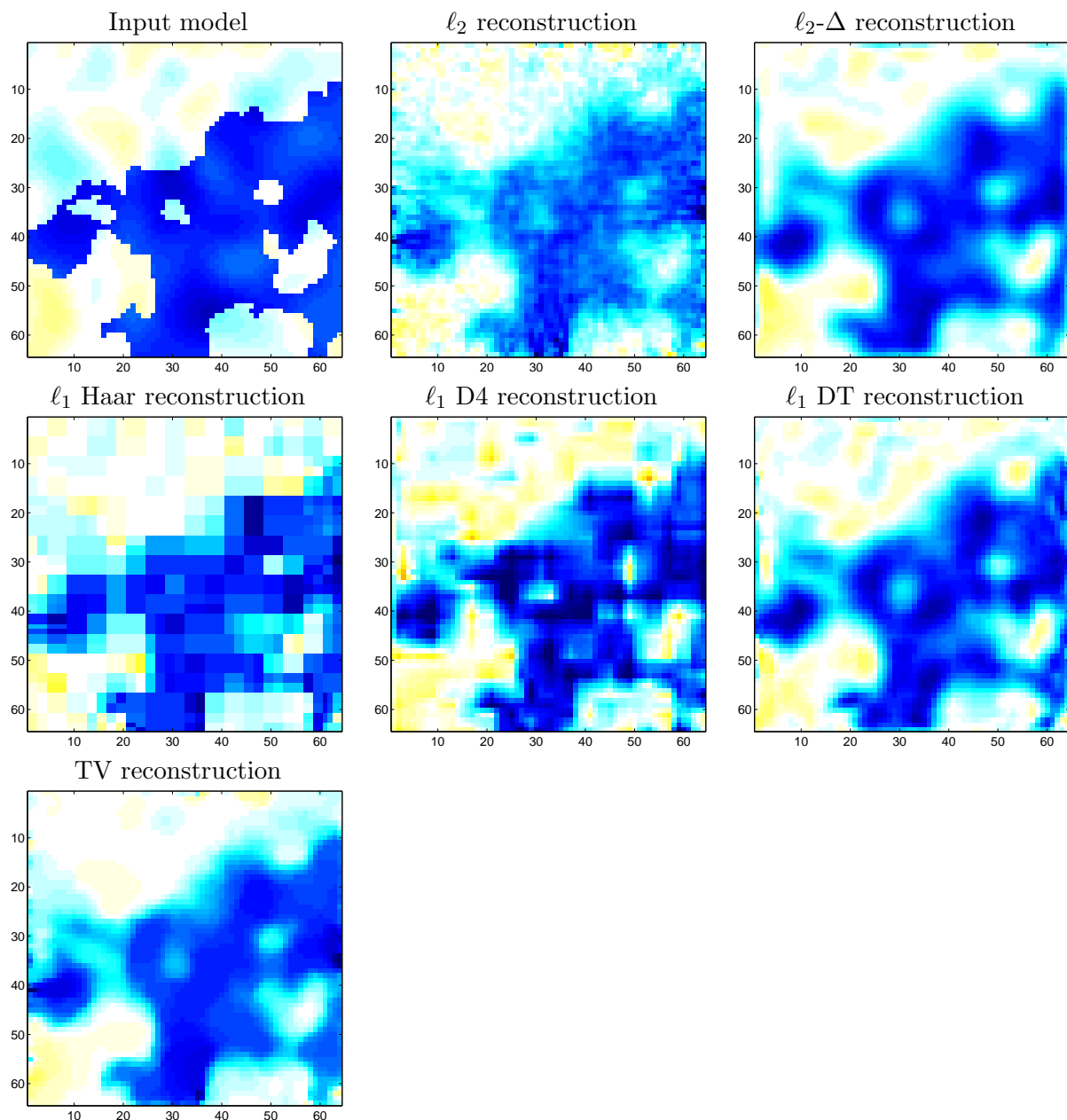


Figure 8: A blow-up of horizontal slice number 25 of the salt dome model and its various reconstructions using all 24000 kernels. The TV, ℓ_2 - Δ and ℓ_1 DT methods introduce the most smoothing. The ℓ_1 Haar reconstruction has the least smoothing but it is very blocky. A good compromise, in this respect, may be found in the ℓ_1 D4 reconstruction.

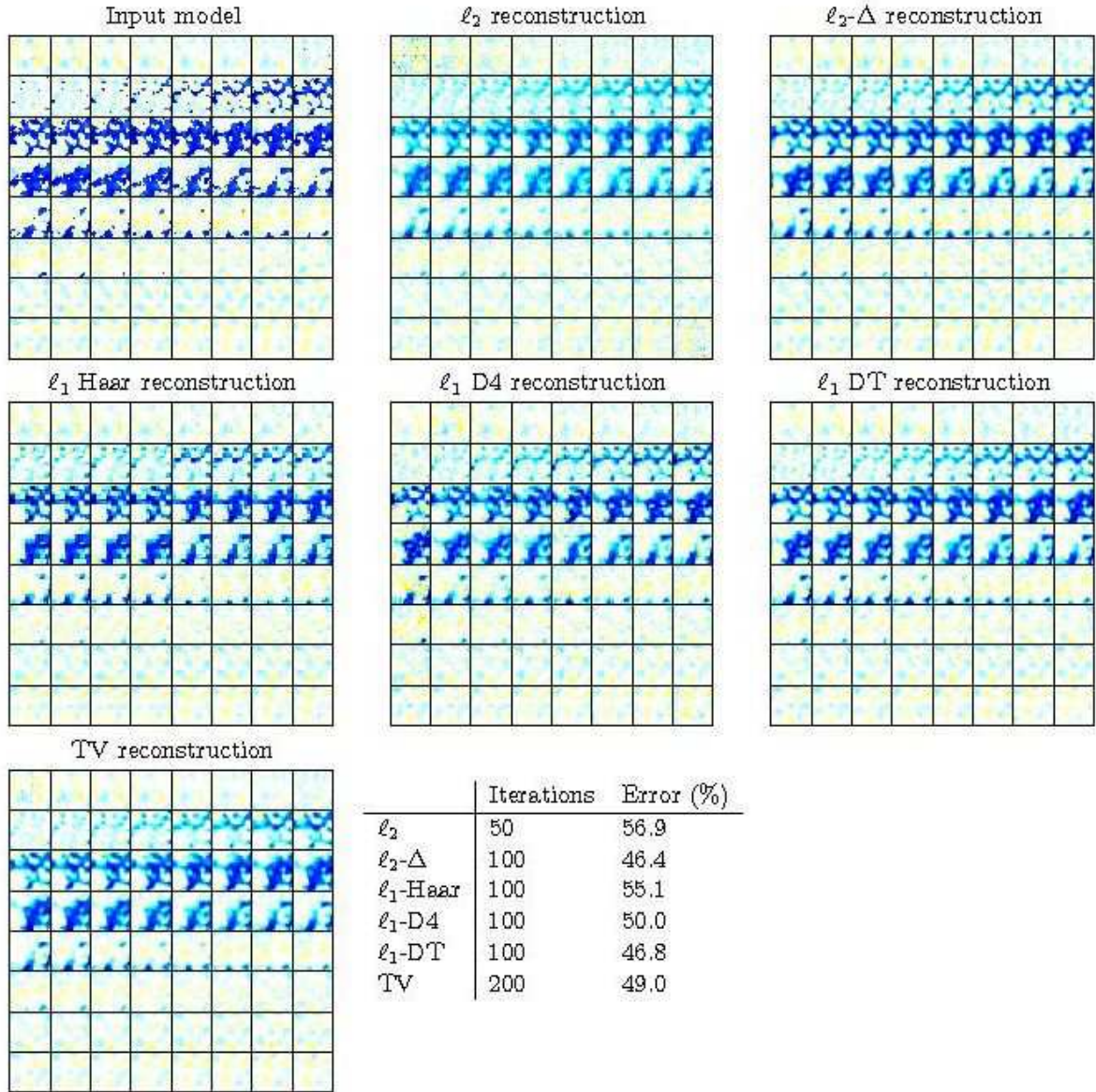


Figure 9: The salt dome model and its reconstructions using only 20000 kernels and thus imperfect coverage. The area of the input model that lies in the region that is not covered by any kernel (white color in figure 2, right), is not well reconstructed. Different methods compensate for this lacking data in different ways. (Note: The arXiv version of this picture uses JPEG compression)

much more complex salt dome model at hand, we must now conclude that this probably represents more a (lucky) exception than a rule. There is no magical solution for the absence of data.

For the checkerboard reconstructions, the ℓ_1 method with Haar wavelets is able to do very well —much better than could be expected based on the data themselves— because the Haar wavelets are very efficient in representing the checkerboard pattern in a sparse way. The success of the ℓ_1 method thus depends heavily on the choice of a suitable basis. For realistic models it is much more difficult to find a good —sparsifying— basis. For the 3D salt dome reconstruction, one could argue that the ℓ_1 -DT method does well because it has good directional sensitivity and is therefore well able to adapt to the “curvy” nature of the outline of the salt body, as opposed to ℓ -Haar and ℓ_1 -D4 methods. The ℓ_2 - Δ method does well because the Gaussian background that is present in the model is smooth ‘noise’ and this is exactly the prior information put into the minimization criterion. The TV method does well as the main part of the salt dome model is roughly piecewise constant and TV favors that.

The wavelets, however, do have the distinctive quality of retaining sharp features even when regularizing by penalizing highly oscillatory models. If the preservation of sharp boundaries is not as important as the correct estimation of amplitudes, the smoothed solution, using the ℓ_2 - Δ method, is to be preferred as it is fully linear and efficient to solve with conjugate gradients. Methods using wavelets with small support, however, are able to retain sharp features, despite their regularization effect that penalizes highly oscillatory models. These methods are thus preferable when edges are important; our preference would go to the ℓ_1 -D4 algorithm which gives less blocky solutions than ℓ_1 -Haar. In no cases should one use simple norm damping (ℓ_2 method).

Speed-wise the nonlinear methods cannot compete with the conjugate gradient algorithm for the ℓ_2 methods. Although many applied mathematics groups (Figueiredo et al., 2008; Bioucas-Dias & Figueiredo, 2007; Elad et al., 2007; Kim et al., 2007; Nesterov, 2007; Hale et al., 2008; Yin et al., 2008) are currently working on speeding up the iterative soft-thresholding algorithm (10), it is still more time-consuming to solve an ℓ_1 -penalized least squares functional than an ℓ_2 -penalized least squares functional, especially for severely ill-conditioned linear systems; Hennenfent et al. (2008) discuss a number of methods in a geophysical context.

Acknowledgments

The authors would like to thank BP America Inc. for kindly providing the 3D salt-dome velocity model. Part of this research has been supported by the Francqui Foundation (IL), the VUB-GOA 62 grant (ID, IL) and NSF grant DMS-0530865 (ID).

References

- Backus, G. & Gilbert, J., 1967. Numerical applications of a formalism for geophysical inverse problems, *Geophysical Journal of the Royal Astronomical Society*, **13**, 247–276.
- Backus, G. & Gilbert, J., 1970. Uniqueness on the inversion of inaccurate gross Earth data, *Philosophical Transactions of the Royal Society of London*, **A266**, 123–192.

- Bioucas-Dias, J. & Figueiredo, M., 2007. A new TwIST: Two-step iterative shrinkage/thresholding algorithms for image restoration, *IEEE Transactions on Image processing*, **16**, 2980–2991.
- Bioucas-Dias, J., Figueiredo, M., & Oliveira, J., 2006. Total variation-based image deconvolution: a majorization-minimization approach, in *IEEE International Conference on Acoustics, Speech and Signal Processing*, vol. 2, pp. 861–864.
- Chevrot, S. & Zhao, L., 2007. Multiscale finite frequency Rayleigh wave tomography of the Kaapvaal craton, *Geophysical Journal International*, **169**, 201–215.
- Cohen, A., Daubechies, I., Jawerth, B., & Vial, P., 1992. Multiresolution analysis, wavelets and fast algorithms on the interval, *Comptes Rendus, Acad. Sc. Paris*, **316**, 417–421.
- Cohen, A., Daubechies, I., & Vial, P., 1993. Wavelets on the interval and fast wavelet transforms, *Journal for Applied and Computational Harmonic Analysis*, **1**, 54–81.
- Dahlen, F. A., 2004. Resolution limit of travelttime tomography, *Geophysical Journal International*, **157**(1), 315–331.
- Daubechies, I., 1992. *Ten lectures on wavelets*, Society for Industrial and Applied Mathematics.
- Daubechies, I., Defrise, M., & De Mol, C., 2004. An iterative thresholding algorithm for linear inverse problems with a sparsity constraint, *Communications On Pure And Applied Mathematics*, **57**(11), 1413–1457.
- Donoho, D., 2006. Compressed sensing, *Information Theory, IEEE Transactions on*, **52**(4), 1289–1306.
- Donoho, D. L., 2006. For most large underdetermined systems of linear equations the minimal ℓ_1 -norm solution is also the sparsest solution, *Comm. Pure Appl. Math.*, **59**, 797–829.
- Elad, M., Matalon, B., & Zibulevsky, M., 2007. Coordinate and subspace optimization methods for linear least squares with non-quadratic regularization, *Applied and Computational Harmonic Analysis*, **23**(3), 346–367.
- Figueiredo, M. A. T., Nowak, R. D., & Wright, S. J., 2008. Gradient projection for sparse reconstruction: Application to compressed sensing and other inverse problems, *IEEE Journal of Selected Topics in Signal Processing (Special Issue on Convex Optimization Methods for Signal Processing)*, **1**, 586–598
- Haar, A., 1910. Zur theorie der orthogonalen funktionensysteme, *Mathematische Annalen*, **69**, 331–371.
- Hale, E., Yin, W., & Zhang, Y., 2008. Fixed-point continuation for ℓ_1 -minimization: Methodology and convergence, Tech. rep., Rice University.
- Hennenfent, G., van den Berg, E., Friedlander, M. P., & Herrmann, F. J., 2008. New insights into one-norm solvers from the Pareto curve, *Geophysics*, **73**(4), A23–A26.

- Kim, S.-J., Koh, K., Lustig, M., Boyd, S., & Gorinevsky, D., 2007. An Interior-Point Method for Large-Scale ℓ_1 -Regularized Least Squares, *IEEE Journal of Selected Topics in Signal Processing*, **1**(4), 606–617.
- Kingsbury, N., 1999. Image processing with complex wavelets, *Philosophical Transactions of the Royal Society A: Mathematical, Physical and Engineering Sciences*, **357**(1760), 2543–2560.
- Kingsbury, N., 2002. Complex wavelets for shift invariant analysis and filtering of signals, *Appl. Computat. Harmon. Anal.*, **10**, 234–253.
- Loris, I., Nolet, G., Daubechies, I., & Dahlen, F. A., 2007. Tomographic inversion using ℓ_1 -norm regularization of wavelet coefficients, *Geophysical Journal International*, **170**(1), 359–370.
- Nesterov, Y., 2007. Gradient methods for minimizing composite objective function, Tech. rep., Ecore. http://www.ecore.be/DPS/dp_1191313936.pdf.
- Nolet, G., 2008. *A Breviary of Seismic Tomography*, Cambridge University Press.
- Tikhonov, A., 1963. Solution of incorrectly formulated problems and the regularization method, *Soviet Math Dokl*, **4**, 1035–1038.
- Yin, W., Osher, S., Goldfarb, D., & Darbon, J., 2008. Bregman iterative algorithms for ℓ_1 -minimization with applications to compressed sensing, *SIAM J. Imaging Sciences*, **1**(1), 143–168.